Constraining light dark matter upscattered by ultrahigh-energy cosmic rays

Chen Xia [a,b], Yan-Hao Xu [a,b], Yu-Feng Zhou [a,b,c,d]

[a] *CAS Key Laboratory of Theoretical Physics, Institute of Theoretical Physics, Chinese Academy of Sciences, Beijing 100190, China*
[b] *University of Chinese Academy of Sciences, Beijing, 100190, China*
[c] *School of Fundamental Physics and Mathematical Sciences, Hangzhou Institute for Advanced Study, UCAS, Hangzhou 310024, China*
[d] *International Centre for Theoretical Physics Asia-Pacific, Beijing/Hangzhou, China*

Abstract

Light halo dark matter (DM) particles upscattered by high-energy cosmic rays (CRs) can be energetic, and become detectable by conventional direct detection experiments. The current constraints derived from space-based direct CR measurements can reach $\mathcal{O}(10^{-31})$ cm^2 for a constant DM-nucleon scattering cross section. We show that if the CR energy spectrum follows a power law of type $\sim E^{-3}$, the derived constraints on the scattering cross section will be highly insensitive to DM particle mass. This suggests that ultrahigh-energy CRs (UHECRs) indirectly measured by ground-based detectors can be used to place constraints on ultralight DM particles, as E^{-3} is a very good approximation of the UHECR energy spectrum up to energy $\sim 10^{20}$ eV. Using the recent UHECR flux data, we show that the current constraints derived from space-based CR measurements can in principle be extended to ultralight DM particles far below eV scale.
© 2021 The Author(s). Published by Elsevier B.V. This is an open access article under the CC BY license (http://creativecommons.org/licenses/by/4.0/). Funded by SCOAP^3.

E-mail address: yfzhou@itp.ac.cn (Y.-F. Zhou).

C. Xia, Y.-H. Xu and Y.-F. Zhou   *Nuclear Physics B ••• (••••) ••••••*

1. Introduction

Although compelling astrophysical evidence supports the existence of dark matter (DM) in the Universe, whether or not DM participates non-gravitational interactions is still an open question. The majority of the current DM direct detection (DD) experiments search for nuclear recoil signals from the scatterings between the halo DM particle and target nucleus. As the typical detection threshold of the current experiments is of $\mathcal{O}(\text{keV})$, searching for light halo DM below GeV is in general challenging. The reason is that for lighter halo DM particles the kinetic energy is lower, and the energy transferred to the target nuclei is suppressed. For instance, for a DM particle with mass $m_\chi \sim 1$ GeV and a typical DM escape velocity $\sim 540 \, \text{km} \, \text{s}^{-1}$, the elastic scattering off a target nucleus with mass ~ 100 GeV leads to a maximal recoil energy ~ 0.06 keV which is significantly lower than the typical detection threshold. Several physical processes have been considered to lower the detection threshold such as using additional photon emission in the inelastic scattering process [1] and the Migdal effect [2,3], etc. The same DM-nucleus scattering process may leave imprints in some cosmological and astrophysical observables, which can be used to place constraints on the scattering cross section. The resulting constraints are in general much weaker but can be applied to lower DM particle masses unreachable to the DD experiments. For instance, from the spectral distortion of the cosmic microwave background (CMB), a constraint of $\sigma_{\chi p} \lesssim 5 \times 10^{-27} \, \text{cm}^2$ for m_χ at 1 keV-TeV can be obtained [4]; the constraints from the population of Milky Way (MW) satellite galaxies can reach $\sigma_{\chi p} \lesssim 6 \times 10^{-30} \, \text{cm}^2$ for $m_\chi \lesssim 10$ keV [5]; and the measurement of the gas cooling rate of the Leo T dwarf galaxy can also lead to a constraint of $\sigma_{\chi p} \lesssim 3 \times 10^{-25} \, \text{cm}^2$ for $m_\chi \lesssim 1$ MeV [6,7].

Recently, it was shown that important constraints can be derived from the scattering between cosmic ray (CR) particles and DM particles in the local Universe. High-energy CR particles in the Galaxy can scatter off halo DM particles, which results in the energy-loss of CRs [8], the production of γ-rays [9,10] and energy-boost of DM particles [11–13], etc. In the last process, a small but irreducible component of DM (referred to as CRDM) can obtain very high kinetic energies. These energetic CRDM particles can scatter again with the target nuclei in underground detectors, and deposit sufficient energy to cross the detection threshold, which greatly extend the sensitivity of the current DD experiments to sub-GeV DM particles [11–18]. It has been shown that in this approach the constraints on constant DM-nucleon (DM-electron) spin-independent scattering cross section can reach $\sim 10^{-31}(10^{-34}) \, \text{cm}^2$ for DM particle mass down to at least ~ 0.1 MeV (~ 1 eV) [11,12] (for constraints on energy-dependent cross sections, see e.g. [14, 15]).

It is of interest to explore the potential of this approach in constraining even lighter DM particles far below MeV scale, as some well-motivated DM candidates such as QCD axions and axion-like particles can be extremely light. Constraining lighter DM requires better information on the CR spectra at higher energies. Note, however, that all the current analysis [11–18] on the detection of CRDM adopted the CR fluxes from either the parametrizations in [19,20] or the GALPROP code [21,22], which are inferred from the space-based direct CR measurements (e.g. PAMELA [23,24], AMS-02 [25,26] and CREAM-I [27] etc.). For current space-based experiments the CR fluxes which can be measured with reasonable precision are typically with energy $\lesssim 200$ TeV (see also the data of CREAM-III [28], CALET [29] and DAMPE [30]). Towards higher energies, the statistic uncertainties increase rapidly due to the limited acceptance of space-based experiments [31–33]. Naively extrapolating these analyses to higher energies will leads to incorrect conclusions, as the spectral feature of the CR flux start to change above 1 PeV. Alternatively, high-energy CR can be measured indirectly by ground-based air-shower detectors.

Despite larger uncertainties in energy scale and mass resolution, this approach can measure the CR flux to much higher energy due to the huge acceptances. For detecting lighter DM particles, the local DM number density is higher. However, the energy transfer from the scattering process becomes less efficient, and the CR flux is known to decrease rapidly towards higher energies. Whether or not ultrahigh-energy CRs (UHECRs, defined as CR with total energy $E >$ PeV) can be used to place useful constraints on ultralight DM will depend strongly on the spectral feature of the UHECR flux.

In this work, we show that as long as the energy spectrum of CR flux follows a power law $\sim E^{-\alpha}$ with $\alpha \lesssim 3$, the derived constraints on the DM-nucleon scattering cross section will not decrease towards lower DM mass. In the limit of $\alpha = 3$, the constraints will DM mass independent. This justifies using UHECR to place stringent constraints on ultralight DM particles, as the UHECR all-particle spectrum above the "knee" structure (at ~ 3 PeV) can be well-approximated by a power law with $\alpha \approx 3$. From the recent UHECR nucleus flux data, we obtain the following results: the constraints on the spin-independent DM-nucleon scattering cross section can be $\lesssim 10^{-(32-31)}$ cm^2 for DM particle mass down to extremely small value $\sim 10^{-12}$ eV, which expands the currently known constraints derived from space-based direct CR measurements by around ten orders of magnitude in DM mass, and close a large previously unconstrained parameter space; the most stringent constraints are found to be at DM mass $\sim 10^{-5}$ eV and $\sim 10^{-11}$ eV, due to the "knee" and "toe" structure in the UHECR flux, respectively; this CRDM approach will completely loss sensitivity for DM mass below 10^{-14} eV as the UHECR flux is highly suppressed above $\sim 10^{20}$ eV, phenomena possibly related to the scatterings between UHECRs and cosmic microwave background (CMB) photons [34,35]. The constraints obtained in this work are highly model-independent and conservative, as only the elastic scattering process is required and very conservative choices of parameters are adopted. The constraints obtained in this work are derived based on the observables of the present-day local Universe, which are complementary to other constraints derived from the data of earlier epochs of the Universe.

This paper is organized as follows: In section 2, we discuss the spectral feature of the DM flux upscattered by UHECRs. In section 3, we discuss the effect of earth attenuation of the CRDM kinetic energy. The nuclear recoil spectrum and the constraints from direct detection experiment Xenon-1T are discussed in section 4. We summarize the work and give some remarks in section 5.

2. CR-upscattered dark matter flux

2.1. Single CR component case

In the generic process of elastic scattering between an incident particle A with kinetic energy T_A and a target particle B at rest, the recoil energy of particle B in the laboratory frame is given by $T_B = T_B^{\max}(1 - \cos\theta)/2$, where θ is the scattering angle of particle B in the center-of-mass (CM) frame. The maximal recoil energy of particle B is given by

$$\frac{T_B^{\max}}{T_A} = \left[1 + \frac{(m_B - m_A)^2}{2m_B(T_A + 2m_A)}\right]^{-1}, \tag{1}$$

where $m_{A(B)}$ is the mass of particle $A(B)$. We assume that the scattering is isotropic in the CM frame, such that the differential cross section $d\sigma_{AB}/dT_B$ in the laboratory frame is simply related to the total cross section σ_{AB} as $d\sigma_{AB}/dT_B = \sigma_{AB}/T_B^{\max}$. In the case of CR-DM scattering, if the CR particle i ($i =$ H, He, ...) is highly relativistic, i.e., the Lorentz factor $\gamma_i \approx T_i/m_i \gg 1$, but m_χ is small enough such that $\gamma_i \ll m_i/2m_\chi$, the maximal recoil energy of the CRDM can

be approximated as $T_\chi^{\max} \approx 2m_\chi \gamma_i^2$. The CRDM particle with kinetic energy T_χ can scatter again with the nucleus N (with mass m_N) in either the outer crust of Earth or the detector of the underground DM direct detection experiments. The maximal recoil energy $T_N^{\max}$ of the nucleus which is also the maximal energy-loss of CRDM particle can be well approximated as $T_N^{\max} \approx 2T_\chi^2/m_N$. Note that $T_N^{\max}$ is independent of DM particle mass.

After being upscattered, the CRDM particles travel through the Galaxy in straight lines as they are not deflected by the interstellar magnetic fields. The observed flux (number of particles per unit area, time and solid angle, $dN/dA dt d\Omega$) of CRDM at the surface of Earth can be approximately written as

$$\frac{d\Phi_\chi}{dT_\chi} \approx \frac{\rho_\chi^{\mathrm{loc}} \sigma_{\chi i} D_{\mathrm{eff}} F^2(Q_\chi^2)}{m_\chi} \int\limits_{\gamma_i^{\min}(T_\chi)}^{\infty} \frac{d\gamma_i}{T_\chi^{\max}} \frac{d\Phi_i^{\mathrm{LIS}}}{d\gamma_i}, \tag{2}$$

where $d\Phi_i^{\mathrm{LIS}}/d\gamma_i$ is the local interstellar CR flux measured at Earth. The integration lower limit $\gamma_i^{\min} \approx (T_\chi/2m_\chi)^{1/2}$ is the minimal Lorentz factor required to produce T_χ. The form factor $F(Q_\chi^2)$ is evaluated at the momentum transfer $Q_\chi^2 = 2m_\chi T_\chi$. For very light DM, $F(Q_\chi^2) \approx 1$ is an excellent approximation. In the above expression we have assumed that the CR energy spectrum in the Galactic halo is not significantly different from that in the local interstellar (LIS) region, i.e., $d\Phi_i(r)/d\gamma_i \approx d\Phi_i^{\mathrm{LIS}}/d\gamma_i$. In this case, the information of halo DM density distribution can be parameterized into a single parameter D_{eff}

$$D_{\mathrm{eff}} \equiv \frac{1}{4\pi \rho_\chi^{\mathrm{loc}}} \int\limits_{\mathrm{l.o.s}} \rho_\chi \, ds \, d\Omega, \tag{3}$$

where $\rho_\chi^{\mathrm{loc}} \approx 0.3$ GeV/cm^3 is the local DM density in the Solar system, and the integration is performed along the line-of-sight (l.o.s). For typical DM profiles, the value of D_{eff} is around a few kpc. In this work, we make a conservative choice of $D_{\mathrm{eff}} = 1$ kpc as a benchmark value.

Let us start with a simple case where the flux of a CR species i can be parametrized by a single power law with index α_i and a cutoff at a Lorentz factor $\gamma_{i,\mathrm{cut}}$ as follows

$$\frac{d\Phi_i^{\mathrm{LIS}}}{d\gamma_i} = \Phi_i^0 \gamma_i^{-\alpha_i} \exp\left(-\frac{\gamma_i}{\gamma_{i,\mathrm{cut}}}\right), \tag{4}$$

where Φ_i^0 is a normalization factor. The power-law behavior is expected if CRs are accelerated by the diffusive shock waves of the Galactic supernova-remnants (SNRs) and the pulsar wind, etc., and the cutoff represents the maximal energy that can be achieved by the acceleration process. If m_χ is sufficiently small such that $\gamma_{i,\mathrm{cut}} \ll m_i/2m_\chi$, which is easily justified for sub-eV CRDM, the approximation of $T_\chi^{\max} \approx 2m_\chi \gamma_i^2$ can be used in the whole integration range of Eq. (2), and the corresponding CRDM flux can be obtained analytically as follows

$$\frac{d\Phi_\chi}{dT_\chi} = \frac{\sigma_{\chi i} \rho_\chi^{\mathrm{loc}} D_{\mathrm{eff}} \Phi_i^0 F^2}{2m_\chi^2 \gamma_{i,\mathrm{cut}}^{\alpha_i+1}} \Gamma(-(\alpha_i+1), t), \tag{5}$$

where Γ is the incomplete Γ-function, $t = (T_\chi/T_{\chi,\mathrm{cut}}^{\max})^{1/2}$ with $T_{\chi,\mathrm{cut}}^{\max} = 2m_\chi \gamma_{i,\mathrm{cut}}^2$ the maximal energy of CRDM upscattered by UHECR at the cutoff $\gamma_{i,\mathrm{cut}}$.

In the region far below the cutoff, i.e., $T_\chi \ll T_{\chi,\mathrm{cut}}^{\max}$, which corresponds to the case where the CR flux is essentially a single power law $\sim T_i^{-\alpha_i}$. Using the asymptotic behavior of the incomplete Γ-function $\Gamma(a, z) \to -z^a/a$ for $z \ll 1$, the CRDM flux can be approximated as

$$\frac{d\Phi_\chi}{dT_\chi} \approx \frac{2\sigma_{\chi i}\rho_\chi^{\text{loc}}D_{\text{eff}}\Phi_i^0 F^2}{\alpha_i + 1} T_\chi^{-2} \left(\frac{T_\chi}{2m_\chi}\right)^{(3-\alpha_i)/2} . \tag{6}$$

As $F(Q_\chi^2) \approx 1$ is a very good approximation for ultralight DM, the above expression shows that the CRDM flux follows a power law $\sim T_\chi^{-(1+\alpha_i)/2}$. The mass dependence of the CRDM flux is proportional to $m_\chi^{(\alpha_i-3)/2}$, which shows that as long as the CR flux is hard enough, namely, $\alpha_i \lesssim 3$, the resulting CRDM flux will not decrease with decreasing DM mass.

Note that in a wide energy range the CR flux is close to the case of $\alpha_i \approx 3$. Direct and indirect measurements show that from a few GeV up to the "knee" (at ~ 3 PeV), the primary CR all-particle spectrum approximately follows a single power law with index $\alpha_i \approx 2.7$. Above the "knee" the spectrum softens to $\alpha_i \approx 3.1$. Before reaching the highest observed energy $\sim 10^{20}$ eV, there are several minor spectral structures such as the "second knee" at $\sim 10^{17}$ eV, the "ankle" at $\sim 8 \times 10^{18}$ eV and the "toe" at $\sim 3 \times 10^{19}$ eV. The corresponding power-law indices vary around the $\alpha_i \approx 3$ case. Consequently, the DM upscattered by UHECR in this ultrahigh-energy region should fluctuate around the power law T_χ^{-2}, and is highly insensitive to DM mass; and the recoil event rate and the derived bounds on $\sigma_{\chi i}$ should be independent of m_χ as well, as the recoil energy or the energy loss in the χN scattering is almost independent of DM mass. Eq. (6) also suggests that the CR electrons are less efficient in constraining ultralight DM particles, as the CR electron flux follows a power law with power index $\alpha_e \approx 4$ after ~ 0.9 TeV [36–38].

In a different region where T_χ is close to the cutoff $T_{\chi,\text{cut}}^{\text{max}}$, the effect of cutoff in CR flux will be significant. Using the asymptotic behavior of $\Gamma(a,z) \to z^{a-1}e^{-z}$ for large z, the CRDM flux is given by

$$\frac{d\Phi_\chi}{dT_\chi} \approx \frac{\sigma_{\chi i}\rho_\chi^{\text{loc}}D_{\text{eff}}\Phi_i^0 F^2}{2m_\chi^2 \gamma_{i,\text{cut}}^{\alpha_i+1}} \left(\frac{T_\chi}{T_{\chi,\text{cut}}^{\text{max}}}\right)^{-\frac{\alpha_i+2}{2}} e^{-\left(\frac{T_\chi}{T_{\chi,\text{cut}}^{\text{max}}}\right)^{1/2}} . \tag{7}$$

Since $T_{\chi,\text{cut}}^{\text{max}}$ is proportional to m_χ, lighter CRDM particles will have an earlier cutoff. A final cutoff in the CR flux around $\sim 10^{20}$ eV is expected from the inelastic scattering between UHECR particles and CMB photons as predicted by Greisen, Zatsepin and Kuzmin [34,35], which is supported by recent observations [39–41]. The cutoff in the UHECR flux essentially sets the scale of the minimal m_χ that can be constrained by this approach.

2.2. Multiple CR component case

The primary CR flux in the ultrahigh-energy region may receive contributions from different sources such as SNRs, pulsar winds and active galactic nuclei (AGN), etc. (for recent reviews see e.g. [42–44]). The multi-source description is also essential to reproduce the observed various spectral structures of UHECRs. Thus a realistic description of the UHECR flux necessarily contains multiple components, which can be written as $\Phi_i = \sum_j \Phi_{ij}$ with $j = 1, \ldots, n$. For each component j, the flux Φ_{ij} takes the form of Eq. (4) with the power index α_i and cutoff $\gamma_{i,\text{cut}}$ replaced by α_{ij} and $\gamma_{ij,\text{cut}}$, respectively. Thus we adopt the following form of the primary CR flux [45]

$$\frac{d\Phi_i^{\text{LIS}}}{d\gamma_i} = \sum_{j=1}^{n} \Phi_{ij}^0 \gamma_i^{-\alpha_{ij}} \exp\left[-\frac{\gamma_i}{\gamma_{ij,\text{cut}}}\right], \tag{8}$$
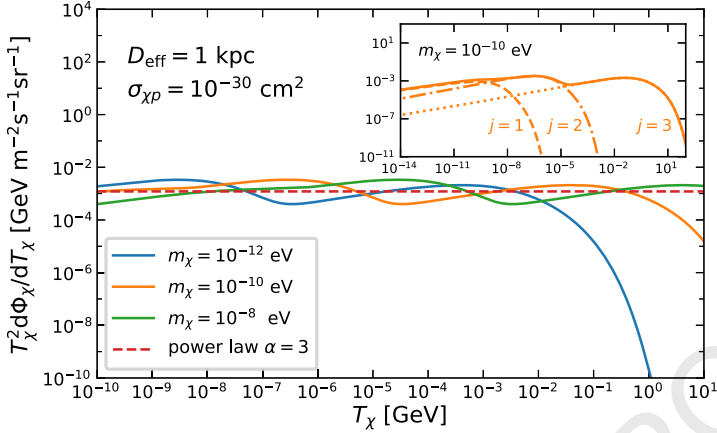
Fig. 1. (solid lines) CRDM flux rescaled by T_χ^2 as a function of kinetic energy with cross section $\sigma_{\chi p} = 10^{-30}\,\mathrm{cm}^2$ for different CRDM masses. The spectral structure in the flux is due to the three-component nature of the parametrization of CR [45]. The inset shows the contribution from each individual CR component ($j = 1, 2, 3$) for the case of $m_\chi = 10^{-10}\,\mathrm{eV}$. The simple case where the CR is proton dominant and follows a single power-law with index $\alpha = 3$ and $\Phi^0 = 2.6 \times 10^2\,\mathrm{cm}^{-2}\,\mathrm{s}^{-1}\mathrm{sr}^{-1}$ is also shown (horizontal dashed line) for comparison. (For interpretation of the colors in the figure(s), the reader is referred to the web version of this article.)

where Φ_{ij}^0 and α_{ij} are the normalization factors and power indices, respectively, for a CR species i in the component j. Following the reasoning of Peters [46], the CR species in each component j should share a common cutoff in rigidity R_j, which leads to $\gamma_{ij,\mathrm{cut}} = (Z_i/m_i)R_j$, where Z_i is the electric-charge of the CR species i. In Ref. [45] four different parametrizations are found to be in good agreement with the current UHECR data [39,47–57]. We choose one of the "Global-Fit" parametrization with $n = 3$. The best-fit values of the rigidity cutoffs are $R_{1,2,3} = 120$ TV, 4 PV and 1.3 EV, respectively [45]. Compared with other parametrizations, this one is the most economic and conservative as the final cutoff of R_3 is the lowest, which leads to the lowest CRDM flux at high energy region. The details of the parametrizations are summarized in Appendix-A.

2.3. DM flux from ultrahigh-energy CRs

Fig. 1 shows the CRDM flux calculated numerically from Eqs. (1) and (2) without using approximations. In the calculation we take the dipole form factors for light CR species H and He [58], and the Helm form factor for heavier species [59,60]. In the energy region where T_χ is far below the lowest cut off, since $\alpha \approx 2.7$ the CRDM fluxes follow an approximate power law $\sim T_\chi^{-1.85}$ and scale with DM mass as $m_\chi^{-0.15}$ which is a rather weak m_χ-dependence. Thus lighter CRDM particle has slightly larger flux. In the cutoff dominated region, due to the superposition of various cutoffs $\gamma_{ij,\mathrm{cut}}$ in the three components, the CRDM fluxes fluctuate around the power law case of T_χ^{-2} over many orders of magnitude in kinetic energy before reaching the last cutoff, and are insensitive to m_χ, which is expected from Eq. (6) and can be clearly seen in Fig. 1. Above the final cutoff R_3, the CRDM flux drops rapidly; the flux of lighter CRDM particle drops faster, as expected from Eq. (7). Taking the case of $m_\chi = 10^{-10}\,\mathrm{eV}$ as an example, the CR protons in the three components lead to the induced CRDM flux with three cut off at $T_{\chi,\mathrm{cut}}^{\max} = 3.3 \times 10^{-9}$, 3.6×10^{-6} and $0.38\,\mathrm{GeV}$, respectively, as can be seen from the inset of Fig. 1. If the cutoff is too

low, the CRDM cannot be energetic enough to produce enough recoil energy to be detected by the DD experiments. Thus a lower limit on m_χ for a given DD experiment exists.

3. Earth attenuation

Before arriving at the underground detectors, CRDM may loss a non-negligible fraction of energy due to the same elastic scatterings with nucleus within the outer crust of Earth. We adopt an analytic approach for Earth attenuation based on average energy loss [61,62]. For simplicity, we only consider elastic scatterings which is an irreducible process and neglect the effect of form factor. The decrease of T_χ with depth z due to the elastic scattering with the nucleus N in Earth's crust is given by

$$\frac{dT_\chi}{dz} = -\sum_N \left(\frac{\rho_N}{m_N}\right) \int_0^{T_N^{\max}} T_N \frac{d\sigma_{\chi N}}{dT_N} dT_N, \tag{9}$$

where ρ_N is the mass density of nucleus N in the crust, and T_N stands for the nucleus recoil energy which equals the energy loss of the incident CRDM particle. Using the expression of $T_N^{\max}$ the energy loss can be approximated as

$$\frac{dT_\chi}{dz} \approx -\kappa T_\chi^2, \tag{10}$$

where $\kappa = \sum_N \rho_N \sigma_{\chi N}/m_N^2$. We consider the case where the scattering is isospin conserving, namely, $\sigma_{\chi n} \approx \sigma_{\chi p}$ such that the cross sections at nucleus and nucleon level are simply related by $\sigma_{\chi N} \approx A_N^2 \sigma_{\chi p}$ with A_N the nucleus mass number of N. We further adopt the relation $m_N \approx A_N m_p$ which is a very good approximation. Under these two simplifications, the factor A_N cancels out in the expression of κ, which gives $\kappa \approx \sigma_{\chi p} \rho_\oplus / m_p^2$ with $\rho_\oplus \approx 2.7\,\mathrm{g \cdot cm^{-3}}$ the average mass density of Earth's outer crust [63]. After integrating Eq. (9), the CRDM kinetic energy T_χ^z at depth z is related to that at surface as

$$\frac{T_\chi}{T_\chi^z} \approx \frac{1}{1 - z\sigma_{\chi p}\rho_\oplus T_\chi^z/m_p^2}. \tag{11}$$

Thus the effect of energy loss is independent of both m_χ and the chemical composition of the crust. For a small enough cross section $\sigma_{\chi p} \ll m_p^2/(z\rho_\oplus T_\chi^z)$, one obtains $T_\chi^z \approx T_\chi$. In the opposite case where $\sigma_{\chi p}$ is large enough, T_χ^z will stop tracking T_χ, and reach a maximal value $T_\chi^{z,\max} \approx m_p^2/z\sigma_{\chi p}\rho_\oplus$ with increasing T_χ. The appearance of $T_\chi^{z,\max}$ is due to the rapid energy loss proportional to T_χ^2 for relativistic incident particles, which leads to a sharp cutoff in the CRDM flux at depth z. The CRDM flux $d\Phi_\chi/dT_\chi^z$ at depth z can be evaluated from that at surface $d\Phi_\chi/dT_\chi$ through the relation $d\Phi_\chi/dT_\chi^z = (d\Phi_\chi/dT_\chi)(dT_\chi/dT_\chi^z)$.

4. Direct detection

4.1. Recoil event spectrum

The differential nuclear recoil event rate per target nucleus mass $\Gamma = dN/dM_N dt dT_N$ of the χN scattering at depth z is given by

$$\Gamma = \frac{4\pi \sigma_{\chi N} F^2(Q_N^2)}{m_N} \int_{T_\chi^{z,\min}(T_N)}^{\infty} \frac{dT_\chi^z}{T_N^{\max}(T_\chi^z)} \frac{d\Phi_\chi}{dT_\chi^z}, \tag{12}$$

where $Q_N^2 = 2m_N T_N$. The scale of T_χ^z relevant to direct detection is set by the lower limit of the integration $T_\chi^{z,\min}(T_N) \approx (T_N m_N/2)^{1/2}$. For a detector located at depth $z \sim 1\,\mathrm{km}$ and a target nucleus mass $m_N \sim 100\,\mathrm{GeV}$, in order to produce a recoil energy T_N which is close to the threshold $T_N^{\mathrm{thr}} \sim 1\,\mathrm{keV}$, the required minimal T_χ^z is $\sim 10\,\mathrm{MeV}$. Thus the condition of $T_\chi^z \approx T_\chi$ leads to a typical requirement of $\sigma_{\chi p} \ll \mathcal{O}(10^{-27})\,\mathrm{cm}^2$. Since the lower bounds of the excluded cross section are expected to be much smaller $\sigma_{\chi p} \lesssim 10^{-31}\,\mathrm{cm}^2$ [11], in deriving the lower bound of the excluded $\sigma_{\chi p}$, the effect of Earth attenuation can be safely neglected. Using the CRDM flux from Eq. (5), the recoil event rate can be written as

$$\Gamma = \frac{\pi \sigma_{\chi N} \sigma_{\chi i} \rho_\chi^{\mathrm{loc}} D_{\mathrm{eff}} \Phi_i^0 F^2}{2m_\chi^3 \gamma_{i,\mathrm{cut}}^{\alpha+3}} \left[-\Gamma(-3-\alpha_i, t') + \frac{\Gamma(-1-\alpha_i, t')}{t'^2} \right],$$

where $t' = [m_N T_N/(8m_\chi^2 \gamma_{i,\mathrm{cut}}^4)]^{1/4}$. In the case where the CR flux follows a power law with index α_i, the recoil event rate can be obtained analytically from Eqs. (6) and (12) as follows

$$\Gamma \approx \frac{\pi \sigma_{\chi N} \sigma_{\chi i} \rho_\chi^{\mathrm{loc}} D_{\mathrm{eff}} \Phi_i^0 F^2}{(1+\alpha_i)(3+\alpha_i)m_N^3} \left(\frac{m_N}{m_\chi}\right)^{\frac{3-\alpha_i}{2}} \left(\frac{T_N}{8m_N}\right)^{-\frac{3+\alpha_i}{4}}, \tag{13}$$

which explicitly shows that if $\alpha_i \lesssim 3$, the recoil event rate is proportional to $T_N^{-3/2}$ and does not decrease with a decreasing m_χ. For the case $\alpha_i \approx 3$, the derived upper limit on $\sigma_{\chi p}$ will be insensitive to m_χ. In Fig. 2, we show the full numerical results of recoil event rate of the scattering between the CRDM particles and xenon nuclei. The approximate power-law behavior of the recoil spectrum can be clearly seen for $T_N \lesssim \mathrm{keV}$. Above $\sim 10\,\mathrm{keV}$, the suppression due to the Helm form factor is visible. Due to the power-law like spectrum of the recoil event rate, the experiment with lower threshold T_N^{thr} will be more sensitive to lighter DM particles.

For large enough cross sections, the appearance of $T_\chi^{z,\max}$ leads to a cutoff in the recoil event spectrum. If the corresponding recoil energy is below the threshold T_N^{thr}, it will form a blind spot for direct detection. This possibility is illustrated in the inset of Fig. 2, which will lead to m_χ-independent upper bounds on the excluded value of $\sigma_{\chi p}$.

4.2. Xenon-1T detector response and data analysis

We numerically calculate excluded regions in the $(m_\chi, \sigma_{\chi P})$ plane at 90% C.L. for CRDM from the data of Xenon-1T experiment located at depth $z \approx 1.4\,\mathrm{km}$ [64,65]. The Xenon-1T experiment utilizes the liquid xenon time projection chambers to detect the recoil energy of the target nuclei from their scattering with DM particles. The deposited energy can produce a prompt scintillation signal (S1) and ionization electrons which are extracted into gaseous xenon and produce proportional scintillation light (S2). The S2/S1 signal size ratio allows for discrimination between nuclear recoils and electron recoils. Since the nuclear recoil event rate from the collisions with CRDM is quite different from that with the nonrelativistic halo DM, to be more accurate on the effect of threshold, we derive the limits directly from the distribution of the signals of S1 and S2, rather than naively rescaling the reported experimental limits from halo WIMP searches [11,13–15].
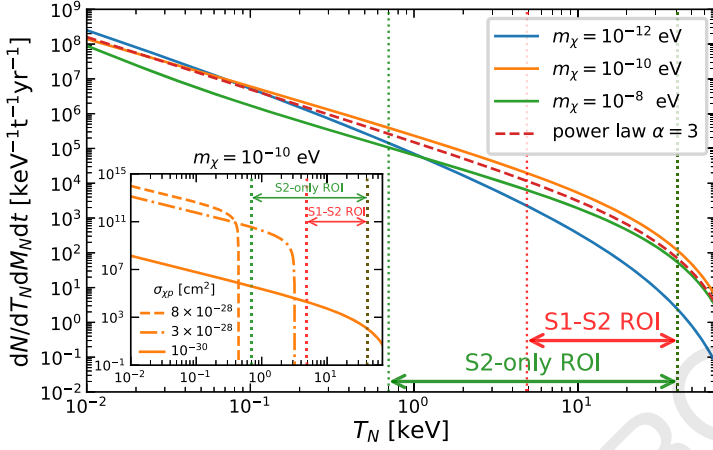
Fig. 2. Recoil event rates of the scattering between CRDM particles and target Xenon nuclei with different DM masses. The value of $\sigma_{\chi p}$ and D_{eff} are the same as that in Fig. 1. The inset shows the recoil rate at different cross sections for $m_\chi = 10^{-10}$ eV. The vertical dotted lines indicate the region-of-interest (ROI) considered by the Xenon-1T experiments for the S1-S2 [64] and S2-only analyses [65].

For the calculations from the deposited recoil energy T_N to the position-corrected signals cS1 and cS2$_b$, we closely follow Ref. [66]. For a deposited recoil energy T_N, the averaged number of photons $\langle N_\gamma \rangle$ and charges $\langle N_e \rangle$ are given by

$$\frac{\langle N_\gamma \rangle}{T_N} = \frac{L}{W} \cdot \frac{\langle r \rangle + \langle N_{ex}/N_i \rangle}{1 + \langle N_{ex}/N_i \rangle}$$

$$\frac{\langle N_e \rangle}{T_N} = \frac{L}{W} \cdot \frac{1 - \langle r \rangle}{1 + \langle N_{ex}/N_i \rangle}, \tag{14}$$

where W is the average energy required to create either an excitation or ion-electron pair in the liquid xenon, L is the Lindhard factor, N_{ex}/N_i is the excitation-to-ion ratio and r is the recombination probability. The prompt and scintillation light hitting the PMT photocathode will produce photoelectrons (PEs). The average number of PEs observed per emitted photon is described by the gain factor $g_1'(x, y, z)$, and the amplification factor for charge signal is described by the parameter $g_2'(x, y)$. The S1 and S2 signal are constructed from N_{pe} and N_{prop}. The bias and fluctuations are modeled by Gaussian distribution with Gauss(δ_{s1}, $\Delta\delta_{s1}$) and Gauss(δ_{s2}, $\Delta\delta_{s2}$) respectively. Finally, the spatial dependences of S1 and S2 will be corrected which leads to the signal cS1 and cS2$_b$. The Xenon-1T collaboration has performed the S1+S2 analysis based with an effective exposure of 1 ton-yr. In the analysis the DM search was performed between $3 < \text{cS1} < 70$ PE, corresponding to an average keV$_{nr}$ of $4.9 - 40.9$ keV with an effective exposure of one ton-year [64]. The Xenon-1T collaboration also formed the S2-only analysis with cS2$_b > 150$ PE, corresponding to a threshold of 0.7 keV$_{nr}$ with an effective exposure of 22 ton-days [65].

We calculate the signal distributions of the scattering between CRDM particles and target Xenon nuclei, and derive the excluded regions in $(m_\chi, \sigma_{\chi p})$ plane for the Xenon-1T data (S1+S2) using the binned Poisson statistic approach [67,68]. The distribution of the background events are taken from the Xenon-1T analysis. The calculation procedure, main parameters and extended results with different parametrizations of CR flux are summarized in appendix-B.
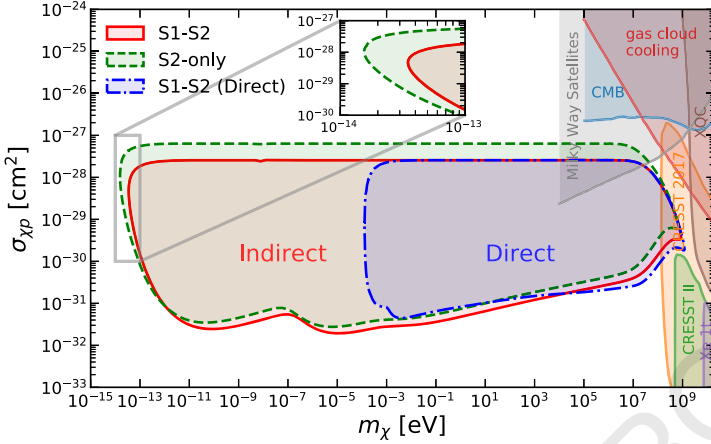
Fig. 3. Exclusion regions in the $(m_\chi, \sigma_{\chi p})$ plane for CRDM. The result using UHECR indirectly measured by ground-based experiments [45] and the Xenon-1T S1-S2 [64] (S2-only [65]) data is shown as a solid (dashed) contour. For comparison, the results using CR directly measured by space-based experiments [19] with a maximal energy of 200 TeV is also shown as a dot-dashed contour. A selection of constraints on halo DM from other experiments such as Xenon-1T [64], CRESST-II [69], CRESST surface run [70], XQC [71] and CMB [72], gas cloud cooling [7], Milky way satellite population [5] are also shown.

4.3. Results

In Fig. 3, we show the final constraints from analyzing the Xenon-1T data. It can be seen from the figure that the lower bound of the excluded region reaches $\sigma_{\chi p} \lesssim 10^{-(32-31)}$ cm² can be extended down to DM particle mass $\sim 10^{-12}$ eV. In the sub-eV region, the shape of the excluded region is directly related to the structures in the UHECR flux. The most stringent limits of $\sigma_{\chi p} \lesssim 3 \times 10^{-32}$ cm² at $m_\chi \sim 10^{-11}$ eV and 10^{-5} eV correspond to the "knee" and the "toe" structures of the UHECR flux. The exclusion region closes at $m_\chi \sim 10^{-14}$ eV, which corresponds to the observed suppression of the UHECR flux at $\sim 10^{20}$ eV possibly due to the GZK cutoff. For comparison purpose, in Fig. 3 we also show the results using the CR proton and Helium fluxes in [19] which are based on the space-based direct CR measurements and are only available for energy below 200 TeV [25,27,73]. It can be seen that using the ground-based indirect UHECR measurements can extend the previous constraints by about ten orders of magnitude towards lower DM particle mass. The constraints are conservative, as we adopted the "Global-Fit" parametrization of the UHECR flux. For other parametrizations such as "H3a", "H4a" and "Global-Fit4", the resulting constraints are even stronger towards lower DM mass, as it is shown in Fig. 6 of Appendix C.

As it can be seen in the inset of Fig. 3, we also find that the constraints on the lowest CRDM mass are very sensitive to the detector threshold as the recoil event spectrum from CRDM is quite different from halo DM. Due to the lower threshold $\sim 0.7\,\mathrm{keV_{nr}}$ of the S2-only data [65], the constraints from the S2-only data which has an exposure about an order of magnitude smaller than that of the S1-S2 data (with a threshold of $\sim 4.9\,\mathrm{keV_{nr}}$ [64]) turns out to be more sensitive to lighter CRDM below 10^{-12} eV.

In the simple analytic approach adopted in this work, the upper bound of the excluded region due to the Earth attenuation is found to be $\sigma_{\chi p} \lesssim 8 \times 10^{-28}$ cm², and is almost insensitive to m_χ, as expected from the fast energy loss proportional to T_χ^2 in Earth attenuation discussed in Sec. 3.

5. Discussions/conclusions

In summary, we have derived novel constraints on ultralight DM boosted by UHECRs. The constraints obtained in this work are highly model independent, as only the DM-nucleon scattering cross section is relevant. The approach only requires the information of the present-day local Universe, even the standard cosmology is not assumed. Thus the constraints are complementary to that derived from different epochs of the Universe, such as the observations of CMB [4,72,74,75], Lyman-α forest [76] and 21 cm radiations [74], etc. If the ultralight DM particles reached chemical and kinetic equilibrium in the early Universe, very stringent constraints will arise from BBN and CMB. However, the conditions for reaching thermal equilibrium require more information on the cross section of DM annihilation and production process, which are in general model dependent. For ultralight DM particles, annihilating into most standard model particles are kinematically forbidden (for the analysis try to connect DM scattering and annihilation cross sections using crossing symmetry, see, e.g. [77]).

In this work, we considered the simplest case where the scattering cross section is a constant, i.e., energy and momentum-transfer independent. For relativistic scatterings, it more likely that the differential scattering cross section depends on the energy of both the incident and outgoing particles. For some simple models, such as the fermionic DM with a scalar mediator, it has been shown that the differential scattering cross section can be greatly enhanced at high momentum transfer. Consequently, the constraints on the total cross section at the zero momentum transfer can be many orders of magnitude stronger for lighter DM particles [15]. The approach proposed in this work can be extended to the case with energy-dependent cross sections in a straight forward manner.

CRediT authorship contribution statement

Chen Xia: Data curation, Formal analysis. **Yan-Hao Xu:** Data curation, Formal analysis. **Yu-Feng Zhou:** Conceptualization, Methodology, Resources, Supervision, Writing – review & editing.

Declaration of competing interest

The authors declare that they have no known competing financial interests or personal relationships that could have appeared to influence the work reported in this paper.

Appendix A. Parametrizations of UHECR flux

CR particles with energy above a few hundred TeV are mainly measured by the ground-based air-shower arrays which detect the cascades of secondary particles from the interactions

Table 1

Normalization constants c_{ij}, power indexes α_{ij}, and rigidity cutoffs R_j in the parametrization of "Global-Fit" and "Global-Fit4" in [45]. The parameters of "Global-Fit4" which are different from those of the "Global-Fit" are shown in parentheses.

		p	He	C	O	Fe	50<Z<56	78<Z<82
$R_1 = 120$ TV	c_{i1}	7000	3200	100	130	60		
	α_{i1}	2.66	2.58	2.4	2.4	2.3		
$R_2 = 4$ PV	c_{i2}	150	65	6	7	2.3 (2.1)	0.1	0.4 (0.53)
	α_{i2}	2.4	2.3	2.3	2.3	2.2	2.2	2.2
$R_3 = 1.3$ (1.5) EV	c_{i3}	14 (12)				0.025 (0.011)		
	α_{i3}	2.4				2.2		
($R_4 = 40$ EV)	c_{i4}	(1.2)						
	α_{i4}	(2.4)						

of primary CR particles in the Earth atmosphere. In such indirect experiments, the information about the chemical composition is limited to determining the relative abundance of the main species or groups. Thus, it is likely that there exist different parametrizations which can describe the data equally well. We take the n-component power-law parametrization in which the CR total energy spectrum of the CR species i has the following form [45]

$$\frac{d\Phi_i^{\mathrm{LIS}}}{dE_i} = \sum_{j=1}^{n} c_{ij} E_i^{-\alpha_{ij}} \exp\left[-\frac{E_i}{Z_i R_j}\right], \tag{A.1}$$

where $j = (1, \ldots, n)$ is the component index, E_i (in unit of GeV) is the total energy of CR species i. The normalization constants c_{ij} are related to Φ_{ij}^0 in Eq. (5) of the main text by $\Phi_{ij}^0 = m_i^{1-\alpha_{ij}} c_{ij}$ where m_i (in unit of GeV) is the mass of CR species i. A global analysis to the recent UHECR data has been performed in [45]. We adopt one of the three-component "Global-Fit" model as the benchmark model with the parameters listed in Table 1. In this parametrization, the first rigidity cutoff R_i is around 100 TV which is the typical maximal energy from the acceleration of SNR with magnetic field around a few μ Gauss. It also well reproduce the observed hardening in the CR all-particle spectrum above 200 GeV [23,78]. In the figure, we also list a slightly extended four-component parametrization (referred to as "Global-Fit4").

Two alternative parametrizations [79] based on the Hillas model [80] are also found in good agreement with data, which are labeled as "H3a" and "H4a" in [45]. The major difference from the "Global-Fit" parametrization is that the first rigidity cutoff is quite high about 4 PV, which is responsible for the "knee" structure. In this type of parametrization the "ankle" represent the transition between the galactic and extra-galactic contributions. The corresponding parameters are listed in Table 2.

The CR all-particle fluxes of the four parametrizations are shown in Fig. 4 together with the recent experiments data.

Appendix B. Xenon-1T data analysis

For the data analysis of the Xenon-1T experiment, we adopt the signal response model described by the Xenon-1T collaboration in [66]. The Xenon-1T experiment utilizes the liquid xenon time projection chambers to detect the recoil energy of the target nuclei from the scatter-

Table 2

Same as Table 1, but for parametrizations of "H3a" and "H4a" in [45]. The parameters of "H4a" which are different from those of "H3a" are shown in parentheses.

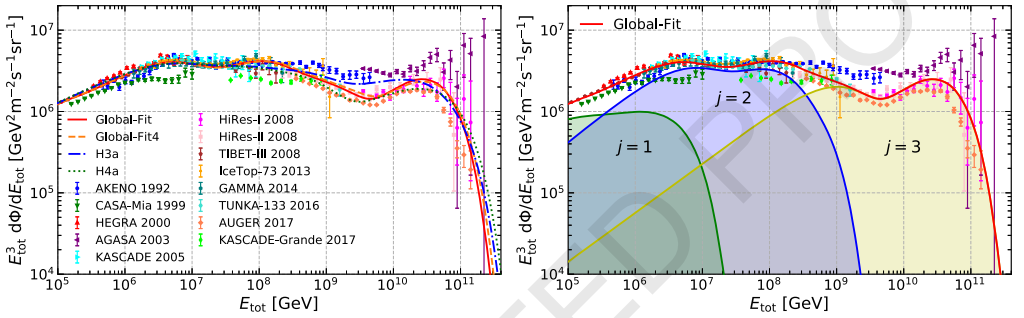|		p	He	CNO	Mg-Si	Fe
$R_1 = 4$ PV	c_{i1}	7860	3550	2200	1430	2120
	α_{i1}	2.66	2.58	2.63	2.67	2.63
$R_2 = 30$ PV	c_{i2}	20	20	13.4	13.4	13.4
	α_{i2}	2.4	2.4	2.4	2.4	2.4
$R_3 = 2$ (60) EV	c_{i3}	1.7 (200)	1.7 (0.0)	1.14 (0.0)	1.14 (0.0)	1.14 (0.0)
	α_{i3}	2.4 (2.6)	2.4	2.4	2.4	2.4

Fig. 4. (Left) CR all-particle spectra for four type of parametrizations in [45] together with the current experimental data [39,47–57]. Right) Contributions from the three individual components in the "Global-Fit" parametrization in [45].

ing with DM particles. The deposited energy can produce a prompt scintillation light signal (S1), and the ionization electrons extracted from liquid xenon into gaseous xenon can produce pro-portional scintillation light (S2). The S2/S1 signal size ratio allows for discrimination between nuclear recoil (NR) and electron recoil (ER) events. For a deposited recoil energy T_N, the pro-duced total number of quantum N_q is the sum of the number of excitons N_{ex} and ion-electron pairs N_i, which follows a binomial distribution $N_q \sim \text{Binom}(T_N/W, L)$ where $W = 13.8$ eV is the average energy required to create either an exciton or ion-electron pair in the liquid xenon, and L is the Lindhard factor. In the case of NR, it is given by [81]

$$L = \frac{k\, g(\epsilon)}{1 + k\, g(\epsilon)}, \tag{B.1}$$

where k is a normalization factor, the function $g(\epsilon)$ is proportional to the ratio of electric and nuclear stopping power, which can be parametrized as $g(\epsilon) = 3\epsilon^{0.15} + 0.7\epsilon^{0.6} + \epsilon$, where $\epsilon = 11.5(T_N/\text{keV})Z^{-7/3}$ with $Z = 54$ the atomic number of the xenon nucleus. The distribution of N_i is described by a binomial distribution $N_i \sim \text{Binom}(N_q, 1/(1 + \langle N_{ex}/N_i \rangle))$, where $\langle N_{ex}/N_i \rangle$ is the averaged exciton-to-ion ratio. The number of excitons is given by $N_{ex} = N_q - N_i$. The excitons contribute to scintillation photon signals through de-excitation process. The ionized electrons have a probability of r to be recombined into xenon atoms and produce scintillation photons, and a probability of $(1-r)$ to escape the ion-electron pair. Thus the number of escaped electrons is given by $N_e \sim \text{Binom}(N_i, 1-r)$ and the total number of photons is $N_\gamma = N_{ex} + N_i - N_e$. The recombination probability r is modeled by a Gaussian distribution $r \sim \text{Gauss}(\langle r \rangle, \Delta r)$,

C. Xia, Y.-H. Xu and Y.-F. Zhou   *Nuclear Physics B ••• (••••) ••••••*

where $\langle r \rangle$ is the mean value and Δr is the variance. The mean value is calculated using the Thomas-Imel box model [82,83]

$$\langle r \rangle = 1 - \frac{\ln(1 + N_i \varsigma/4)}{N_i \varsigma/4}, \tag{B.2}$$

where $\varsigma = 0.057 F^{-0.12}$ with $F = 81$ V/cm the electric field. The variance is described by $\Delta r = q_2(1 - e^{-T_N/q_3})$ with $q_2 = 0.034$ and $q_3 = 1.7$. In summary, the averaged number of photons $\langle N_\gamma \rangle$ and charges $\langle N_e \rangle$ are given by

$$\frac{\langle N_\gamma \rangle}{T_N} = \frac{L}{W} \cdot \frac{\langle r \rangle + \langle N_{ex}/N_i \rangle}{1 + \langle N_{ex}/N_i \rangle},$$

$$\frac{\langle N_e \rangle}{T_N} = \frac{L}{W} \cdot \frac{1 - \langle r \rangle}{1 + \langle N_{ex}/N_i \rangle}. \tag{B.3}$$

The photon and charge signals are converted into photoelectron (PE) emission of the photomultiplier tube (PMT) photocathode. The corresponding gain factors are: $g_1'(x, y, z)$ the average number of PEs observed per emitted photon, and $g_2'(x, y)$ the amplification factor for charge signals. Both are spatial dependent.

The spatial-dependence of the signals S1 and S2 are corrected, which results in the corrected signals $cS1$ and $cS2_b$ (corresponding to the S2 signals from the bottom PMTs). These two quantities can be understood as spatial-averaged signals. For simplicity we use the spatial-averaged gain factors of $g_1 = 0.142$ and $g_2 = 11.4$ for $cS1$ and $cS2_b$, respectively. Thus in this case the number of PE is given by $N_{pe} \sim \text{Binom}(N_\gamma, g_1)$ and that of proportional signal is given by $N_{prop} \sim \text{Gauss}(N_e g_2, \sqrt{N_e}\Delta g_2)$, with $\Delta g_2/g_2 = 0.25$. The $cS1$ and $cS2_b$ signals are constructed from N_{pe} and N_{prop}. The biases and fluctuations in the construction process are modeled as

$$cS1/N_{pe} - 1 \sim \text{Gauss}(\delta_{s1}, \Delta\delta_{s1}), \tag{B.4}$$

$$cS2_b/N_{prop} - 1 \sim \text{Gauss}(\delta_{s2}, \Delta\delta_{s2}), \tag{B.5}$$

where we adopt mean values of $\delta_{s1(s2)} = -0.065\,(0.034)$, and variances $\Delta\delta_{s1(s2)} = 0.110\,(0.030)$.

$$\langle cS1 \rangle \approx \frac{T_N \cdot L}{W} \frac{\langle r \rangle + \langle N_{ex}/N_i \rangle}{1 + \langle N_{ex}/N_i \rangle} g_1 \cdot (1 + \delta_{s1}),$$

$$\langle cS2_b \rangle \approx \frac{T_N \cdot L}{W} \frac{1 - \langle r \rangle}{1 + \langle N_{ex}/N_i \rangle} g_2 \cdot (1 + \delta_{s2}). \tag{B.6}$$

In the left panel of Fig. 5, we show the Monte Carlo (MC) simulation of the signal distributions from a typical scattering between non-relativistic halo DM and xenon nucleus for $m_\chi = 200$ GeV and $\sigma_{\chi p} = 4.7 \times 10^{-47}$ cm^2. We adopt the Maxwellian distribution of the standard halo model (SHM) for DM with the most probable velocity $v_0 = 220$ km/s, the escape velocity $v_{esc} = 544$ km/s, the local DM density $\rho_\chi^{loc} = 0.3$ GeV/cm^3 and the Earth velocity $v_E = 232$ km/s [84]. We assume the scattering process is elastic, spin-independent and isospin-conserving, and adopt the Helm form factor [60]. We find that the figure is in reasonable agreement with the result of the Xenon-1T collaboration [64].

For deriving the constraints on $\sigma_{\chi p}$ from halo DM, we consider two different two statistic methods. The first one is the Binned Poisson (BP) method [67,68]. First, let us consider the single-bin case. Given an expectation value of $\lambda = b + s$ events with s the theoretical prediction and b the expected background, the probability of observing N_{obs} events is given by the Poisson distribution
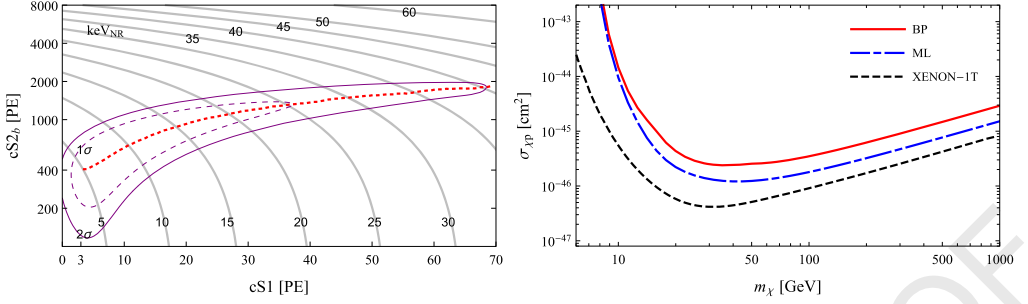
Fig. 5. Left) Nuclear recoil signal distributions from halo DM-Xe scattering with $m_\chi = 200$ GeV and $\sigma_{\chi p} = 4.7 \times 10^{-47}$ cm^2, through MC simulation. The purple dashed and purple solid are 1σ and 2σ percentiles of DM signal, and the central value (red dashed) is shown for reference. The gray lines are the iso-energy contours in keV$_{nr}$. Right) 90% C.L. upper limit on $\sigma_{\chi p}$ from DM of SHM by two different statistic approaches described above, binned Poisson (BP, red solid) maximum likelihood (ML, blue dot-dashed). We also show the result from XENON-1T (black dashed) for comparison.

$$P(N_{obs}|\lambda) = \text{Poiss}(N_{obs}|\lambda). \tag{B.7}$$

The value of λ_p at which $P(\lambda > \lambda_p|N_{obs})$ is smaller than α is excluded at $1 - \alpha$ confidence level (C.L.). For example, the 90% C.L. exclusion limit means $\alpha = 0.1$. The required λ_p can be obtained from $P(\lambda > \lambda_p|N_{obs}) = P(N < N_{obs}|\lambda_p) < \alpha$. In the case of multiple bins, if $(1 - \alpha_{\text{bin}})$ is the probability of seeing $\lambda < \lambda_p$ in that bin, the possibility $(1 - \alpha)$ of seeing $\lambda < \lambda_p$ in any of the bins is given by the binomial distribution

$$1 - \alpha = (1 - \alpha_{\text{bin}})^{N_{\text{bin}}}, \tag{B.8}$$

where N_{bin} is the number of bins. For a desired exclusion level of $1 - \alpha$, we then use this relation to determine α_{bin}, and find the value of λ_p.

The second one is the Maximal Likelihood (ML) method. In this method, the joint likelihood is obtained by the product of individual likelihoods in each bin i, i.e., $\mathcal{L} = \prod_i \mathcal{L}_i$ where $\mathcal{L}_i = \text{Poiss}(N_{obs}|\lambda_i)$ is the Poisson distribution. The theoretical prediction of the event number depends on DM parameters, e.g. $\lambda_i = \lambda_i(m_\chi, \sigma_{\chi p})$ The test statistics is defined as

$$\text{TS} = -2\ln\frac{\mathcal{L}(m_\chi, \sigma_{\chi p})}{\mathcal{L}(\hat{m}_\chi, \hat{\sigma}_{\chi p})}, \tag{B.9}$$

where $\hat{m}_\chi$ and $\hat{\sigma}_{\chi p}$ are the best-fit DM parameters which maximize the likelihood. For a given value of m_χ, the TS should approximately follow a χ^2-distribution with one degree-of-freedom [85]. The value of σ_χ for which TS > 2.7 are excluded at 90% C.L.

For the S1-S2 combined data analysis, the Xenon-1T collaboration adopted the energy regions of interest (ROI) for cS1 as $3 < $cS1$ < 70$ PE, corresponding to an average energy of 4.9–40.9 keV$_{nr}$. The ROI for cS2$_b$ is $50.1 < $cS2$_b < 7940$ PE. The selection of ROIs affects the total acceptance. We take the total acceptance due to the data selection, reconstruction, noise rejection, S1-S2 correlation and single scattering, etc. from Fig. 14 of [86]. In deriving the constraints on CRDM, we use the data of cS2$_b$ distribution shown in Fig. 4 of [64]. In the figure the distribution is shown with respect to the rescaled quantity (cS2$_b - \mu_{\text{ER}})/\sigma_{\text{ER}}$, where μ_{ER} and σ_{ER} are the ER mean and 1σ quantile, respectively. We take $\mu_{\text{ER}} = 1958$ PE and $\sigma_{\text{ER}} = 408$ PE from the cS2$_b$ distribution shown in Fig. 3 of [64]. The number of signal counts s_i in a given bin of cS2$_b$ signal is given by
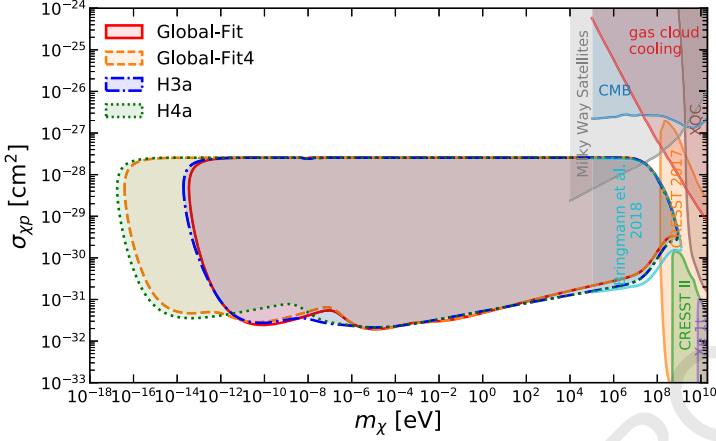
Fig. 6. Exclusion regions in the $(m_\chi, \sigma_{\chi p})$ plane from the Xenon-1T data on the S1-S2 signals and four CR parameterizations.

$$s_i = E_X \int_{(cS2_b)_i^{\text{low}}}^{(cS2_b)_i^{\text{up}}} d\langle cS2_b \rangle \frac{dN}{dT_N} \frac{dT_N}{d\langle cS2_b \rangle} \epsilon_2(\langle cS2_b \rangle), \tag{B.10}$$

where $E_X = 1$ tone · year is the total exposure of the XENON-1T data, $(cS2_b)_i^{\text{low(up)}}$ is the lower (upper) endpoints of the i-th bin of the corresponding $cS2_b$ signal. $\epsilon_2 = A_1(cS1)A_2(cS2_b)$ is the total efficiency of $cS2_b$, where $A_{1,2}$ are the acceptance within the ROI of $cS1$ and $cS2_b$, respectively, and are vanishing outside the ROIs. The value of $\langle cS1 \rangle$ and $\langle cS2_b \rangle$ are related to each other through Eq. (B.6), so the total efficiency of S2 can be written as a function of $\langle cS2_b \rangle$ only. For the background event number b_i, we directly adopt the overall expected background given by XENON-1T, which include electric recoils, neutron, surface, accidental coincidence (AC), and coherent elastic neutrino-nucleus scatters (CEνNS).

In the right panel of Fig. 5 we show the upper limits on $\sigma_{\chi p}$ at 90% C.L. for SHM DM using the BP and ML statistic methods. The DM local density and velocity distribution are the same as that for Fig. 5. In the figure, the limits obtained by the Xenon-1T collaboration using a full profile likelihood analysis are also shown for comparison. It can be seen that the limits obtained in BP and ML approaches are quite conservative. As we are interested in conservative constraints on CRDM properties, we adopt the BP statistic approach in the main text.

Using the relation between the S2 signal and the averaged recoil energy for NR and ER process shown in Fig. 6 of the supplementary material of [65], we convert the Xenon-1T S2-only data in Fig. 4 Ref. [65] into the NR recoil energy distribution dN/dT_N. The total number of events in the i-th energy bin is given by For s_i, we have

$$s_i = \int_{(T_N)_i^{\text{low}}}^{(T_N)_i^{\text{up}}} dT_N \frac{dN}{dt_N} \epsilon_{\text{ex}}(T_N), \tag{B.11}$$

where $(T_N)_i^{\text{low(up)}}$ is the lower (upper) endpoints of the i-th energy bin, and $\epsilon_{\text{ex}}(T_N)$ is the effective exposure which is a function of recoil energy T_N shown in Fig. 1 of Ref. [65]. For the

background event number, we use the expected background given by XENON-1T, which include cathode, CEvNS, flat ER background for S2-only data.

Appendix C. Excluded regions for CRDM

Making use of the Xenon-1T S1-S2 data, we derive the excluded regions in $(m_\chi, \sigma_{\chi p})$ plane using the BP statistic approach for the four different parametrizations of the primary CR flux. The results are shown in Fig. 6. It can be seen that the constraints based on the "Global-Fit" parametrization are quite conservative compared with other parametrizations.

References

[1] C. Kouvaris, J. Pradler, Probing sub-GeV dark matter with conventional detectors, Phys. Rev. Lett. 118 (3) (2017) 031803, arXiv:1607.01789 [hep-ph].

[2] M. Ibe, W. Nakano, Y. Shoji, K. Suzuki, Migdal effect in dark matter direct detection experiments, J. High Energy Phys. 03 (2018) 194, arXiv:1707.07258 [hep-ph].

[3] M.J. Dolan, F. Kahlhoefer, C. McCabe, Directly detecting sub-GeV dark matter with electrons from nuclear scattering, Phys. Rev. Lett. 121 (10) (2018) 101801, arXiv:1711.09906 [hep-ph].

[4] V. Gluscevic, K.K. Boddy, Constraints on scattering of keV–TeV dark matter with protons in the early universe, Phys. Rev. Lett. 121 (8) (2018) 081301, arXiv:1712.07133 [astro-ph.CO].

[5] E.O. Nadler, V. Gluscevic, K.K. Boddy, R.H. Wechsler, Constraints on dark matter microphysics from the milky way satellite population, Astrophys. J. Lett. 878 (2) (2019) 32, arXiv:1904.10000 [astro-ph.CO]; Erratum: Astrophys. J. Lett. 897 (2020) L46; Erratum: Astrophys. J. 897 (2020) L46.

[6] D. Wadekar, G.R. Farrar, First astrophysical constraints on dark matter interactions with ordinary matter at low relative velocity, arXiv:1903.12190 [hep-ph].

[7] A. Bhoonah, J. Bramante, F. Elahi, S. Schon, Calorimetric dark matter detection with galactic center gas clouds, Phys. Rev. Lett. 121 (13) (2018) 131101, arXiv:1806.06857 [hep-ph].

[8] C.V. Cappiello, K.C. Ng, J.F. Beacom, Reverse direct detection: cosmic ray scattering with light dark matter, Phys. Rev. D 99 (6) (2019) 063004, arXiv:1810.07705 [hep-ph].

[9] R.H. Cyburt, B.D. Fields, V. Pavlidou, B.D. Wandelt, Constraining strong baryon dark matter interactions with primordial nucleosynthesis and cosmic rays, Phys. Rev. D 65 (2002) 123503, arXiv:astro-ph/0203240.

[10] D. Hooper, S.D. McDermott, Robust constraints and novel gamma-ray signatures of dark matter that interacts strongly with nucleons, Phys. Rev. D 97 (11) (2018) 115006, arXiv:1802.03025 [hep-ph].

[11] T. Bringmann, M. Pospelov, Novel direct detection constraints on light dark matter, Phys. Rev. Lett. 122 (17) (2019) 171801, arXiv:1810.10543 [hep-ph].

[12] Y. Ema, F. Sala, R. Sato, Light dark matter at neutrino experiments, Phys. Rev. Lett. 122 (18) (2019) 181802, arXiv:1811.00520 [hep-ph].

[13] C. Cappiello, J.F. Beacom, Strong new limits on light dark matter from neutrino experiments, Phys. Rev. D 100 (10) (2019) 103011, arXiv:1906.11283 [hep-ph].

[14] J.B. Dent, B. Dutta, J.L. Newstead, I.M. Shoemaker, Bounds on cosmic ray-boosted dark matter in simplified models and its corresponding neutrino-floor, Phys. Rev. D 101 (11) (2020) 116007, arXiv:1907.03782 [hep-ph].

[15] K. Bondarenko, A. Boyarsky, T. Bringmann, M. Hufnagel, K. Schmidt-Hoberg, A. Sokolenko, Direct detection and complementary constraints for sub-GeV dark matter, J. High Energy Phys. 03 (2020) 118, arXiv:1909.08632 [hep-ph].

[16] S.-F. Ge, J.-L. Liu, Q. Yuan, N. Zhou, Boosted diurnal effect of sub-GeV dark matter at direct detection experiment, arXiv:2005.09480 [hep-ph].

[17] B.-L. Zhang, Z.-H. Lei, J. Tang, Constraints on cosmic-ray boosted DM in CDEX-10, arXiv:2008.07116 [hep-ph].

[18] W. Wang, L. Wu, J.M. Yang, H. Zhou, B. Zhu, Sub-GeV gravity-mediated dark matter in direct detections, arXiv: 1912.09904 [hep-ph].

[19] S. Della Torre, et al., From observations near the Earth to the local interstellar spectra, in: 25th European Cosmic Ray Symposium, 12 2016, arXiv:1701.02363 [astro-ph.HE].

[20] D. Bisschoff, M. Potgieter, O. Aslam, New very local interstellar spectra for electrons, positrons, protons and light cosmic ray nuclei, Astrophys. J. 878 (1) (2019) 59, arXiv:1902.10438 [astro-ph.HE].

[21] A. Strong, I. Moskalenko, Propagation of cosmic-ray nucleons in the galaxy, Astrophys. J. 509 (1998) 212–228, arXiv:astro-ph/9807150.

[22] I. Moskalenko, A. Strong, Production and propagation of cosmic ray positrons and electrons, Astrophys. J. (2021), arXiv:astro-ph/9710124.

[23] PAMELA Collaboration, O. Adriani, et al., PAMELA measurements of cosmic-ray proton and helium spectra, Science 332 (2011) 69–72, arXiv:1103.4055 [astro-ph.HE].

[24] O. Adriani, et al., Time dependence of the proton flux measured by PAMELA during the July 2006 - December 2009 solar minimum, Astrophys. J. 765 (2013) 91, arXiv:1301.4108 [astro-ph.HE].

[25] AMS Collaboration, M. Aguilar, et al., Precision measurement of the proton flux in primary cosmic rays from rigidity 1 GV to 1.8 TV with the alpha magnetic spectrometer on the international space station, Phys. Rev. Lett. 114 (2015) 171103.

[26] AMS Collaboration, M. Aguilar, et al., Precision measurement of the helium flux in primary cosmic rays of rigidities 1.9 GV to 3 TV with the alpha magnetic spectrometer on the international space station, Phys. Rev. Lett. 115 (21) (2015) 211101.

[27] Y. Yoon, et al., Cosmic-ray proton and helium spectra from the first CREAM flight, Astrophys. J. 728 (2011) 122, arXiv:1102.2575 [astro-ph.HE].

[28] Y. Yoon, et al., Proton and helium spectra from the CREAM-III flight, Astrophys. J. 839 (1) (2017) 5, arXiv:1704.02512 [astro-ph.HE].

[29] CALET Collaboration, O. Adriani, et al., Direct measurement of the cosmic-ray proton spectrum from 50 GeV to 10 TeV with the calorimetric electron telescope on the international space station, Phys. Rev. Lett. 122 (18) (2019) 181102, arXiv:1905.04229 [astro-ph.HE].

[30] DAMPE Collaboration, Q. An, et al., Measurement of the cosmic-ray proton spectrum from 40 GeV to 100 TeV with the DAMPE satellite, Sci. Adv. 5 (9) (2019), eaax3793, arXiv:1909.12860 [astro-ph.HE].

[31] B. Nilsen, et al., Cosmic ray H and He spectra from 2-TeV/nucleon to 800-TeV/nucleon from the JACEE experiments, AIP Conf. Proc. 412 (1) (1997) 1031–1034.

[32] RUNJOB Collaboration, V. Derbina, et al., Cosmic-ray spectra and composition in the energy range of 10-TeV - 1000-TeV per particle obtained by the RUNJOB experiment, Astrophys. J. Lett. 628 (2005) L41–L44.

[33] E. Atkin, et al., New universal cosmic-ray knee near a magnetic rigidity of 10 TV with the NUCLEON space observatory, JETP Lett. 108 (1) (2018) 5–12, arXiv:1805.07119 [astro-ph.HE].

[34] K. Greisen, End to the cosmic ray spectrum?, Phys. Rev. Lett. 16 (1966) 748–750.

[35] G.T. Zatsepin, V.A. Kuzmin, JETP Lett. 4 (1966) 78.

[36] H.E.S.S. Collaboration, F. Aharonian, et al., Probing the ATIC peak in the cosmic-ray electron spectrum with H.E.S.S., Astron. Astrophys. 508 (2009) 561, arXiv:0905.0105 [astro-ph.HE].

[37] CALET Collaboration, O. Adriani, et al., Energy spectrum of cosmic-ray electron and positron from 10 GeV to 3 TeV observed with the calorimetric electron telescope on the international space station, Phys. Rev. Lett. 119 (18) (2017) 181101, arXiv:1712.01711 [astro-ph.HE].

[38] DAMPE Collaboration, G. Ambrosi, et al., Direct detection of a break in the teraelectronvolt cosmic-ray spectrum of electrons and positrons, Nature 552 (2017) 63–66, arXiv:1711.10981 [astro-ph.HE].

[39] HiRes Collaboration, R. Abbasi, et al., First observation of the Greisen-Zatsepin-Kuzmin suppression, Phys. Rev. Lett. 100 (2008) 101101, arXiv:astro-ph/0703099.

[40] Pierre Auger Collaboration, A. Castellina, Highlights from the Pierre auger observatory (ICRC2019), PoS ICRC2019 (2020) 004, arXiv:1909.10791 [astro-ph.HE].

[41] Pierre Auger, Telescope Array Collaboration, O. Deligny, The energy spectrum of ultra-high energy cosmic rays measured at the Pierre Auger Observatory and at the Telescope Array, PoS ICRC2019 (2020) 234, arXiv:2001.08811 [astro-ph.HE].

[42] M. Kachelriess, D. Semikoz, Cosmic ray models, Prog. Part. Nucl. Phys. 109 (2019) 103710, arXiv:1904.08160 [astro-ph.HE].

[43] A.A. Watson, High-energy cosmic rays and the Greisen–Zatsepin–Kuz'min effect, Rep. Prog. Phys. 77 (2014) 036901, arXiv:1310.0325 [astro-ph.HE].

[44] M. Nagano, A.A. Watson, Observations and implications of the ultrahigh-energy cosmic rays, Rev. Mod. Phys. 72 (2000) 689–732.

[45] T.K. Gaisser, T. Stanev, S. Tilav, Cosmic ray energy spectrum from measurements of air showers, Front. Phys. (Beijing) 8 (2013) 748–758, arXiv:1303.3565 [astro-ph.HE].

[46] Peters, Nuovo Cimento XXII (1961) 800–819.

[47] M. Nagano, M. Teshima, Y. Matsubara, H. Dai, T. Hara, N. Hayashida, M. Honda, H. Ohoka, S. Yoshida, Energy spectrum of primary cosmic rays above 10**17-eV determined from the extensive air shower experiment at Akeno, J. Phys. G 18 (1992) 423–442.

[48] M. Glasmacher, et al., The cosmic ray energy spectrum between 10**14-eV and 10**16-eV, Astropart. Phys. 10 (1999) 291–302.

[49] HEGRA Collaboration, F. Arqueros, et al., Energy spectrum and chemical composition of cosmic rays between 0.3-PeV and 10-PeV determined from the Cherenkov light and charged particle distributions in air showers, Astron. Astrophys. 359 (2000) 682–694, arXiv:astro-ph/9908202.

[50] M. Takeda, et al., Energy determination in the Akeno Giant Air Shower Array experiment, Astropart. Phys. 19 (2003) 447–462, arXiv:astro-ph/0209422.

[51] KASCADE Collaboration, T. Antoni, et al., KASCADE measurements of energy spectra for elemental groups of cosmic rays: results and open problems, Astropart. Phys. 24 (2005) 1–25, arXiv:astro-ph/0505413.

[52] TIBET III Collaboration, M. Amenomori, et al., The all-particle spectrum of primary cosmic rays in the wide energy range from 10**14 eV to 10**17 eV observed with the Tibet-III air-shower array, Astrophys. J. 678 (2008) 1165–1179, arXiv:0801.1803 [hep-ex].

[53] IceCube Collaboration, M. Aartsen, et al., Measurement of the cosmic ray energy spectrum with IceTop-73, Phys. Rev. D 88 (4) (2013) 042004, arXiv:1307.3795 [astro-ph.HE].

[54] S. Ter-Antonyan, Sharp knee phenomenon of primary cosmic ray energy spectrum, Phys. Rev. D 89 (12) (2014) 123003, arXiv:1405.5472 [astro-ph.HE].

[55] V. Prosin, et al., Results from Tunka-133 (5 years observation) and from the Tunka-HiSCORE prototype, EPJ Web Conf. 121 (2016) 03004.

[56] Pierre Auger Collaboration, F. Fenu, The cosmic ray energy spectrum measured using the Pierre Auger Observatory, PoS ICRC2017 (2018) 486.

[57] KASCADE Grande Collaboration, C.J. Arteaga-Velázquez, et al., Measurements of the muon content of EAS in KASCADE-Grande compared with SIBYLL 2.3 predictions, PoS ICRC2017 (2018) 316.

[58] C. Perdrisat, V. Punjabi, M. Vanderhaeghen, Nucleon electromagnetic form factors, Prog. Part. Nucl. Phys. 59 (2007) 694–764, arXiv:hep-ph/0612014.

[59] R.H. Helm, Inelastic and elastic scattering of 187-mev electrons from selected even-even nuclei, Phys. Rev. 104 (1956) 1466–1475.

[60] J. Lewin, P. Smith, Review of mathematics, numerical factors, and corrections for dark matter experiments based on elastic nuclear recoil, Astropart. Phys. 6 (1996) 87–112.

[61] C. Kouvaris, I.M. Shoemaker, Daily modulation as a smoking gun of dark matter with significant stopping rate, Phys. Rev. D 90 (2014) 095011, arXiv:1405.1729 [hep-ph].

[62] G.D. Starkman, A. Gould, R. Esmailzadeh, S. Dimopoulos, Opening the window on strongly interacting dark matter, Phys. Rev. D 41 (1990) 3594.

[63] R. Rudnick, S. Gao, Composition of the continental crust, in: Treatise on Geochemistry, Pergamon, Oxford, 2003.

[64] XENON Collaboration, E. Aprile, et al., Dark matter search results from a one ton-year exposure of XENON1T, Phys. Rev. Lett. 121 (11) (2018) 111302, arXiv:1805.12562 [astro-ph.CO].

[65] XENON Collaboration, E. Aprile, et al., Light dark matter search with ionization signals in XENON1T, Phys. Rev. Lett. 123 (25) (2019) 251801, arXiv:1907.11485 [hep-ex].

[66] XENON Collaboration, E. Aprile, et al., XENON1T dark matter data analysis: signal and background models and statistical inference, Phys. Rev. D 99 (11) (2019) 112009, arXiv:1902.11297 [physics.ins-det].

[67] A.M. Green, Calculating exclusion limits for weakly interacting massive particle direct detection experiments without background subtraction, Phys. Rev. D 65 (2002) 023520, arXiv:astro-ph/0106555.

[68] C. Savage, G. Gelmini, P. Gondolo, K. Freese, Compatibility of DAMA/LIBRA dark matter detection with other searches, J. Cosmol. Astropart. Phys. 04 (2009) 010, arXiv:0808.3607 [astro-ph].

[69] CRESST Collaboration, G. Angloher, et al., Results on light dark matter particles with a low-threshold CRESST-II detector, Eur. Phys. J. C 76 (1) (2016) 25, arXiv:1509.01515 [astro-ph.CO].

[70] CRESST Collaboration, G. Angloher, et al., Results on MeV-scale dark matter from a gram-scale cryogenic calorimeter operated above ground, Eur. Phys. J. C 77 (9) (2017) 637, arXiv:1707.06749 [astro-ph.CO].

[71] M.S. Mahdawi, G.R. Farrar, Constraints on dark matter with a moderately large and velocity-dependent DM-nucleon cross-section, J. Cosmol. Astropart. Phys. 10 (2018) 007, arXiv:1804.03073 [hep-ph].

[72] W.L. Xu, C. Dvorkin, A. Chael, Probing sub-GeV dark matter-baryon scattering with cosmological observables, Phys. Rev. D 97 (10) (2018) 103530, arXiv:1802.06788 [astro-ph.CO].

[73] AMS Collaboration, M. Aguilar, et al., Observation of the identical rigidity dependence of He, C, and o cosmic rays at high rigidities by the alpha magnetic spectrometer on the international space station, Phys. Rev. Lett. 119 (25) (2017) 251101.

[74] T.R. Slatyer, C.-L. Wu, Early-universe constraints on dark matter-baryon scattering and their implications for a global 21 cm signal, Phys. Rev. D 98 (2) (2018) 023013, arXiv:1803.09734 [astro-ph.CO].

[75] K.K. Boddy, V. Gluscevic, First cosmological constraint on the effective theory of dark matter-proton interactions, Phys. Rev. D 98 (8) (2018) 083510, arXiv:1801.08609 [astro-ph.CO].

[76] R. Murgia, V. Iršič, M. Viel, Novel constraints on noncold, nonthermal dark matter from Lyman-α forest data, Phys. Rev. D 98 (8) (2018) 083540, arXiv:1806.08371 [astro-ph.CO].

[77] G. Krnjaic, S.D. McDermott, Implications of BBN bounds for cosmic ray upscattered dark matter, Phys. Rev. D 101 (12) (2020) 123022, arXiv:1908.00007 [hep-ph].

[78] CREAM Collaboration, H. Ahn, et al., Discrepant hardening observed in cosmic-ray elemental spectra, Astrophys. J. Lett. 714 (2010) L89–L93, arXiv:1004.1123 [astro-ph.HE].

[79] T.K. Gaisser, Spectrum of cosmic-ray nucleons, kaon production, and the atmospheric muon charge ratio, Astropart. Phys. 35 (2012) 801–806, arXiv:1111.6675 [astro-ph.HE].

[80] A. Hillas, Can diffusive shock acceleration in supernova remnants account for high-energy galactic cosmic rays?, J. Phys. G 31 (2005) R95–R131.

[81] B. Lenardo, K. Kazkaz, A. Manalaysay, J. Mock, M. Szydagis, M. Tripathi, A global analysis of light and charge yields in liquid xenon, IEEE Trans. Nucl. Sci. 62 (6) (2015) 3387–3396, arXiv:1412.4417 [astro-ph.IM].

[82] J. Thomas, D. Imel, Recombination of electron-ion pairs in liquid argon and liquid xenon, Phys. Rev. A 36 (1987) 614–616.

[83] M. Szydagis, N. Barry, K. Kazkaz, J. Mock, D. Stolp, M. Sweany, M. Tripathi, S. Uvarov, N. Walsh, M. Woods, NEST: a comprehensive model for scintillation yield in liquid xenon, J. Instrum. 6 (2011) P10002, arXiv:1106.1613 [physics.ins-det].

[84] A. Drukier, K. Freese, D. Spergel, Detecting cold dark matter candidates, Phys. Rev. D 33 (1986) 3495–3508.

[85] W.A. Rolke, A.M. Lopez, J. Conrad, Limits and confidence intervals in the presence of nuisance parameters, Nucl. Instrum. Methods Phys. Res., Sect. A 551 (2005) 493–503, arXiv:physics/0403059.

[86] XENON Collaboration, E. Aprile, et al., XENON1T dark matter data analysis: signal reconstruction, calibration and event selection, Phys. Rev. D 100 (5) (2019) 052014, arXiv:1906.04717 [physics.ins-det].